S. Aghion, C. Amsler, G. Bonomi, R.S. Brusa, M. Caccia, R. Caravita, F. Castelli, G. Cerchiari, D. Comparat, G. Consolati, A. Demetrio, L. Di Noto, M. Doser, C.W. Evans, M. Fani, R.O. Ferragut, J. Fesel, A. Fontana, S. Gerber, M. Giammarchi, A. Gligorova, F. Guatieri, S. Haider, A. Hinterberger, H. Holmestad, A. Kellerbauer, O. Khalidova, D. Krasnicky, V. Lagomarsino, P. Lansonneur, P. Lebrun, C. Malbrunot, S. Mariazzi, J. Marton, V. Matveev, Z. Mazzotta, S.R. Muller, G. Nebbia, P. Nedelec, M. Oberthaler, N. Pacifico, D. Pagano, L. Penasa, V. Petracek, F. Prelz, M. Prevedelli, B. Rienaecker, J. Robert, O.M. Røhne, A. Rotondi, H. Sandaker, R. Santoro, L. Smestad, F. Sorrentino, G. Testera, I.C. Tietje, E. Widmann, P. Yzombard, C. Zimmer, J. Zmeskal, N. Zurlo, M. Antonello
Compression of a Mixed Antiproton and Electron Non-Neutral Plasma to High Densities
European Physical Journal D, Vol. 72, N. 4, 2018, 76 (11 pages)
doi:10.1140/epjd/e2018-80617-x

Eur. Phys. J. D (2018) 72: 76
https://doi.org/10.1140/epjd/e2018-80617-x

THE EUROPEAN PHYSICAL JOURNAL D

Regular Article

Compression of a mixed antiproton and electron non-neutral plasma to high densities

Stefano Aghion[1,2], Claude Amsler[3], Germano Bonomi[4,5], Roberto S. Brusa[6,7], Massimo Caccia[2,8], Ruggero Caravita[9,10], Fabrizio Castelli[2,11], Giovanni Cerchiari[12], Daniel Comparat[13], Giovanni Consolati[1,2], Andrea Demetrio[14], Lea Di Noto[9,10], Michael Doser[15], Craig Evans[1,2], Mattia Fanì[9,10,15], Rafael Ferragut[1,2], Julian Fesel[15], Andrea Fontana[5], Sebastian Gerber[15], Marco Giammarchi[2], Angela Gligorova[3], Francesco Guatieri[6,7], Stefan Haider[15], Alexander Hinterberger[15], Helga Holmestad[16], Alban Kellerbauer[12], Olga Khalidova[15], Daniel Krasnický[10,a], Vittorio Lagomarsino[9,10], Pierre Lansonneur[17], Patrice Lebrun[17], Chloé Malbrunot[3,15], Sebastiano Mariazzi[6,7], Johann Marton[3], Victor Matveev[18,19], Zeudi Mazzotta[2,11], Simon R. Müller[14], Giancarlo Nebbia[20], Patrick Nedelec[17], Markus Oberthaler[14], Nicola Pacifico[15], Davide Pagano[4,5], Luca Penasa[6,7], Vojtech Petracek[21], Francesco Prelz[2], Marco Prevedelli[22], Benjamin Rienaecker[15], Jacques Robert[13], Ole M. Røhne[16], Alberto Rotondi[5,23], Heidi Sandaker[16], Romualdo Santoro[2,8], Lillian Smestad[15,24], Fiodor Sorrentino[10], Gemma Testera[10], Ingmari C. Tietje[15], Eberhard Widmann[3], Pauline Yzombard[12], Christian Zimmer[12,15,25], Johann Zmeskal[3], Nicola Zurlo[5,26], and Massimiliano Antonello[2,8]

[1] Politecnico of Milano, Piazza Leonardo da Vinci 32, 20133 Milano, Italy
[2] INFN Milano, via Celoria 16, 20133 Milano, Italy
[3] Stefan Meyer Institute for Subatomic Physics, Austrian Academy of Sciences, Boltzmanngasse 3, 1090 Vienna, Austria
[4] Department of Mechanical and Industrial Engineering, University of Brescia, via Branze 38, 25123 Brescia, Italy
[5] INFN Pavia, via Bassi 6, 27100 Pavia, Italy
[6] Department of Physics, University of Trento, via Sommarive 14, 38123 Povo, Trento, Italy
[7] TIFPA/INFN Trento, via Sommarive 14, 38123 Povo, Trento, Italy
[8] Department of Science, University of Insubria, Via Valleggio 11, 22100 Como, Italy
[9] Department of Physics, University of Genova, via Dodecaneso 33, 16146 Genova, Italy
[10] INFN Genova, via Dodecaneso 33, 16146 Genova, Italy
[11] Department of Physics, University of Milano, via Celoria 16, 20133 Milano, Italy
[12] Max Planck Institute for Nuclear Physics, Saupfercheckweg 1, 69117 Heidelberg, Germany
[13] Laboratoire Aimé Cotton, Université Paris-Sud, ENS Cachan, CNRS, Université Paris-Saclay, 91405 Orsay Cedex, France
[14] Kirchhoff-Institute for Physics, Heidelberg University, Im Neuenheimer Feld 227, 69120 Heidelberg, Germany
[15] Physics Department, CERN, 1211 Geneva 23, Switzerland
[16] Department of Physics, University of Oslo, Sem Sælandsvei 24, 0371 Oslo, Norway
[17] Institute of Nuclear Physics, CNRS/IN2p3, University of Lyon 1, 69622 Villeurbanne, France
[18] Institute for Nuclear Research of the Russian Academy of Science, Moscow 117312, Russia
[19] Joint Institute for Nuclear Research, 141980 Dubna, Russia
[20] INFN Padova, via Marzolo 8, 35131 Padova, Italy
[21] Czech Technical University in Prague, Břehová 7, 11519 Prague 1, Czech Republic
[22] University of Bologna, Viale Berti Pichat 6/2, 40126 Bologna, Italy
[23] Department of Physics, University of Pavia, via Bassi 6, 27100 Pavia, Italy
[24] The Research Council of Norway, P.O. Box 564, 1327 Lysaker, Norway
[25] Department of Physics, Heidelberg University, Im Neuenheimer Feld 226, 69120 Heidelberg, Germany
[26] Department of Civil Engineering, University of Brescia, via Branze 43, 25123 Brescia, Italy

Received 28 September 2017 / Received in final form 17 January 2018
Published online 30 April 2018

Abstract. We describe a multi-step "rotating wall" compression of a mixed cold antiproton–electron non-neutral plasma in a 4.46 T Penning–Malmberg trap developed in the context of the AEgIS experiment at CERN. Such traps are routinely used for the preparation of cold antiprotons suitable for antihydrogen production. A tenfold antiproton radius compression has been achieved, with a minimum antiproton radius

[a] e-mail: daniel.krasnicky@ge.infn.it

of only 0.17 mm. We describe the experimental conditions necessary to perform such a compression: minimizing the tails of the electron density distribution is paramount to ensure that the antiproton density distribution follows that of the electrons. Such electron density tails are remnants of rotating wall compression and in many cases can remain unnoticed. We observe that the compression dynamics for a pure electron plasma behaves the same way as that of a mixed antiproton and electron plasma. Thanks to this optimized compression method and the high single shot antiproton catching efficiency, we observe for the first time cold and dense non-neutral antiproton plasmas with particle densities $n \geq 10^{13}\,\mathrm{m}^{-3}$, which pave the way for an efficient pulsed antihydrogen production in AEgIS.

1 Introduction

Cold trapped antiproton clouds are instrumental for low energy antimatter research. Since the first efficient production of cold antihydrogen ($\bar{H}$) was achieved [1,2], several experiments are preparing the first precision measurements with $\bar{H}$, such as the measurement of the gravitational behavior of antimatter [3,4] or precise spectroscopy on antihydrogen as a test of the CPT theorem [5,6]. These experimental setups share some common features, including the use of Penning–Malmberg traps to catch, cool and store antiprotons, and it is of great importance to create cold, dense and small radius antiproton clouds. For example, in the case of multipolar combined traps, which are used for simultaneous antiproton and antihydrogen confinement, the radial plasma dimension limits the particle expansion rate and thus the particle heating [7,8]. On the other hand, for experiments like AEgIS, where antihydrogen will be produced by a charge exchange reaction between positronium and cold antiprotons [3], it is necessary to prepare a radially small antiproton cloud to allow for a radially small antiproton trap. This is necessary in order to be able to place the positronium formation target as close as possible to the antiprotons to maximize the antihydrogen production rate.

In this work we show the results and a detailed description of efficient compression of a mixed $\bar{p}$ and e^- non-neutral plasma up to high antiproton peak densities using a "rotating wall" (RW) drive [9]. The RW drive, which is common in experiments with single-component non-neutral trapped plasmas, creates a torque on the plasma and, within an appropriate range of parameters, compression is obtained by increasing the total angular momentum of the rigidly rotating plasma. Many non-neutral plasma RW experiments have been performed in the past, usually with pure electron plasmas or with laser-cooled ion plasmas [9–11]. The theory behind the dynamics of the compression of single or multi-species plasmas with the rotating wall method is rather limited (especially in case of a dipolar field) and, to our knowledge, up to now there is little theoretical work that would allow the experimentalist to use a simple set of formulae to predetermine the compression rate and efficiency inside a trap. Much of the previous work was thus done in a descriptive manner, where some observed effects are partially explained by observing that the torque transfer from the RW drive to the plasma can be attributed to the coupling of the RW signal to the azimuthal Trivelpiece–Gould (standing) waves of the finite-length plasma column (see for example [10]). In the first reported antiproton compression study that used the RW technique on antiprotons and electrons [12], it was shown that the compression of a mixed $\bar{p}$ and e^- plasma is achieved at a fixed frequency if the compression of the electron cloud is slow enough (using low amplitudes). In this paper, we expand on this finding and show that the speed of compression is not the key parameter; rather, full compression of the electron cloud, including its low density radial tails, is central in achieving high radial antiproton compression. The antiproton compression dynamics seems to be solely dependent on the electron dynamics and can thus be optimized outside of the antiproton beamtime. Before discussing the compression technique in Section 4, the initial conditions (Sect. 2) will be presented and the centrifugal separation effect (Sect. 3) addressed, which is an important factor to be avoided in cold non-neutral antiproton plasma compression. We expect that the techniques described here could be further improved in the future to achieve even higher radial compression ratios and improve the overall $\bar{p}$ compression efficiency.

2 Experimental scheme

All measurements described within this work were carried out in the AEgIS experiment's antiproton catching and cooling Penning–Malmberg trap as part of the experimental campaign towards pulsed antihydrogen production. The experimental setup is schematically shown in Figure 1. The so called "P-trap" region of the AEgIS trap system, which was used in the compression studies, is a 12-electrode Penning–Malmberg multi-ring trap with an inner diameter of 30 mm composed of ten 13.5 mm long electrodes and two 30 mm long endcaps at each end. All electrodes can be independently biased with up to ±200 V. Two of the central electrodes are equally cut into four azimuthal sectors onto which the RW radio-frequency (RF) compression signal is summed on top of the respective DC bias potential. The RW drive is a sinusoidal voltage signal $V(t) = A_{\mathrm{RW}} \sin(\omega_{\mathrm{RW}}\, t + \phi)$ of a given frequency $f_{\mathrm{RW}} = \omega_{\mathrm{RW}}/2\pi$ and an amplitude A_{RW}. The sine signal is shifted in phase ϕ by 90 degrees on each azimuthal sector of the electrodes, thus creating an approximation of a rotating dipolar radial field. The trap is located in a cryogenic 10 K UHV bore of a superconducting solenoid, which creates an axial magnetic field of 4.46 T. The P-trap is used to store electrons, antiprotons and positrons.

The particle diagnostics is performed destructively by lowering the endcap voltage, allowing the particles to escape, and by recording the resulting signal on three

types of detectors: a Faraday cup that measures the total electron number; external scintillator detectors that count the number of $\bar{p}$ by comparing the detected signal to a Monte Carlo simulation; and a micro-channel plate (MCP) assembly (Hamamatsu F2223 with a P46 phosphor screen and a digital camera) that can measure the radial profiles of electrons or antiprotons. The MCP is located in a magnetic field of 1 T and at a temperature of ≈40 K. It images only 5 mm radially of the 15 mm radius P-trap, both due to the presence of smaller radius electrodes upstream of the MCP in the 1 T region, and due to particle cloud radial expansion (by a factor of $\sqrt{4.46\,\mathrm{T}/1\,\mathrm{T}}$) caused by the difference in the magnetic fields.

A typical operation cycle starts by loading ≈4×10^8 e^- in a region spanning ten electrodes of the P-trap (with a trapping potential of 140 V, green curve of Figure 2) and then adjusting the electron plasma to radii of ≈1.5 mm by turning on the RW_1 drive[1] with $f_{\mathrm{RW}_1} = 300$–400 kHz, and $A_{\mathrm{RW}_1} = 2$ V. After ≈35 s (while the RW_1 drive is kept on) the antiprotons are caught. Antiprotons at 5.3 MeV kinetic energy delivered by CERN's Antiproton Decelerator (AD) pass through a $53 \pm 3\,\mu$m thick silicon beam monitor and a $173.7 \pm 0.5\,\mu$m thick aluminum "degrader" foil,[2] which acts as the final decelerator where a small fraction of the incoming beam is slowed down below 9 keV and caught by two high voltage (9 kV) electrodes (not shown in Fig. 1) that are located upstream and downstream of the P-trap region. The antiproton catching and cooling trap of AE$\bar{\mathrm{g}}$IS, along with the antiproton catching procedure, is described in greater detail in [13].

The catching efficiency depends mainly on the aluminum foil degrader thickness and the $\bar{p}$ beam position and its intensity. We optimized the degrader thickness to achieve a peak $\bar{p}$ catching efficiency of 1.25% for one AD bunch of 3.6×10^7 antiprotons.

The ∼keV energy antiprotons remain trapped by the high voltages and are gradually cooled down to the ∼eV energy range (and lower) within <50 s by collisions with the previously loaded electrons,[3] which in turn cool down by emission of cyclotron radiation in the strong magnetic field (the calculated cooling time constant of e^- in the absence of $\bar{p}$ is 200 ms [14]). At this stage the high voltage electrodes are ramped to ground potential, releasing the uncooled antiprotons towards the degrader, where their annihilation signal and number is measured by the external scintillators. At the end of the cooling cycle, the cold antiprotons thus remain trapped along with the preloaded electrons in the P-trap region with the RW_1 drive being on for ∼85 s in total, of which 50 s are during the $\bar{p}$ catching and cooling. The $\bar{p}$ cooling efficiency (measured with the external scintillators) ranges from 50% to 60% and mainly depends on the initial antiproton–electron

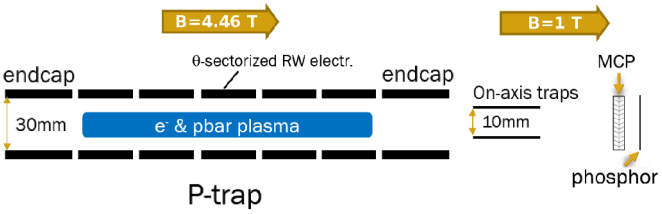

Fig. 1. Schematic of the experimental setup. The antiproton and electron non-neutral plasma is kept in the 4.46 T Penning–Malmberg trap and is then extracted either towards a Faraday cup on the left (not shown) or towards the MCP located inside the 1 T field and behind the smaller radius 1 T traps.

cloud overlap. Thus normally, the number of antiprotons mixed with electrons before the compression experiments is ≈2×10^5 $\bar{p}$.

We then perform various particle manipulations as described later in the text and at the end of each experiment we reshape the trap to a shorter configuration, where the plasma is trapped under five electrodes with two short electrodes acting as endcaps (blue curve in Fig. 2). We then apply five 80 ns long pulses (8.3 μs apart) to the endcaps of this trap that temporarily set the endcap potential to 0 V. This allows the electrons to escape, while the majority of the antiprotons remain trapped due to their lower speed (from the scintillators we see that more than ∼90% of $\bar{p}$ remain trapped). Successively, after 250–500 μs the antiprotons are released from the trap either with ten 2.6 μs long pulses (8.3 μs apart) applied on the right endcap electrode (in Fig. 1) onto the MCP detector, which measures the radial density profile integrated along the magnetic field axis, or by lowering the left (in Fig. 1) endcap voltage and releasing the antiprotons onto the degrader foil, where the antiproton number is counted with the external scintillator detectors. The choice of reshaping the plasma to a shorter trap[4] before the final extraction was necessary due to the impossibility of extracting all electrons from the longer trap without incurring large antiproton losses with an excessive number of e^- extraction pulses. During the various reshaping procedures we do not observe particle losses.

The MCP detector has (due to its digital camera readout) a relatively long dead-time of ∼60 ms and since the antiproton cloud dimensions could vary dramatically shortly after the electron removal, we could not measure at once both the electron and antiproton cloud radial profiles. For this reason we repeat each experiment in the same conditions and in one case we measure the electron radial profile on the MCP (and count the antiprotons on the degrader), while in the other case we measure the antiproton radial profile on the MCP (and count the electrons on the degrader). The response of the MCP detector was verified with dedicated antiproton and electron measurements, where the signal linearity

[1] RW_i indicates the ith RW application (with possibly differing settings) in the particle manipulation procedure.

[2] This aluminum degrader foil is connected to an amplifier and acts as the Faraday cup detector for the electron number readout at later stages of the experiment.

[3] The $\bar{p}$ energy range is indicative; even though it has not been measured, we know that the temperature is in the eV range (or lower) from the absence of cold antiproton losses in similar cooling experiments that used lower trap potentials.

[4] As long as confinement is maintained at every step, the reshaping did not seem to be critical. When moving the plasma to a shorter trap, the potentials are changed one electrode at a time (fastest rate is with steps of 1.5 V/ms). If the trap floor level needs to be changed then all electrodes move together with a typical step of 1.5 V/10 ms.

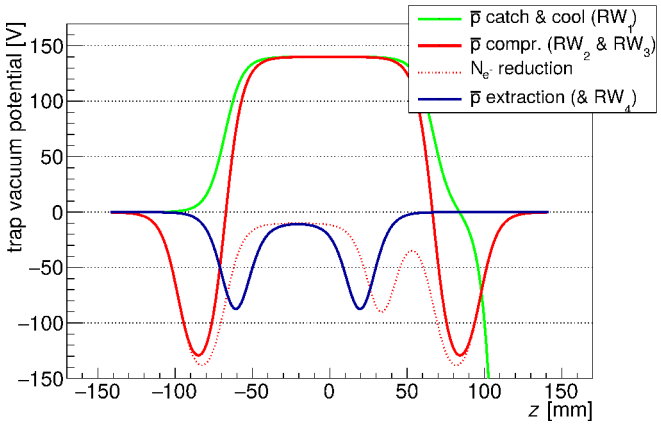

Fig. 2. The on-axis potentials along the z (magnetic field) axis of the P-trap region used during various stages of the compression procedures (described in the text). Displayed are "vacuum" potentials in the absence of plasma space-charge. The two RW electrodes are located at $z = 0$ (P-trap center).

and saturation regimes were identified and the MCP gain dependence on the supply voltages was measured. The MCP front plate was grounded while the MCP bias voltage was in the range 800–1100 V (based on the particle type and density). The phosphor screen was usually operated at 3 kV voltage difference with respect to the MCP output plate.

The measurement procedures described above required a high repeatability from one experimental cycle to another. This was achieved by stable initial electron loading conditions (electron number varied with standard deviation of 2.6%) and by a real-time operating system controlling a custom-built 10 MHz clocked FPGA that deterministically sets the electrode potentials or triggers other hardware. The main instability comes from the antiproton beam parameters, which affect the dynamics during the plasma compression due to the fact that a non-negligible fraction of electrons in the trap are secondary electrons created in the degrader foils and also caught in the high-voltage trap and cooled by the preloaded electrons. The shot-to-shot instability is mainly dependent on both electron and antiproton number and initial size fluctuation and constitutes the main systematic error of our measurements. The scatter of the data points in the presented figures is due to the above mentioned fluctuations of many experimental parameters. Statistical errors of single measurements in most figures are smaller than the size of the symbols.

3 Centrifugal separation of e^- and $\bar{p}$ plasmas

Due to the geometry of the Penning–Malmberg traps, the clouds of trapped charged particles have a cylindrical symmetry with the particle density $n(r, z)$ being a function of the axial and radial coordinates, where the z-axis points along the magnetic field axis and $(r, z) = (0, 0)$ is the cloud center. We call such a cloud of trapped charged particles a (non-neutral) plasma if both the interparticle spacing $n^{-1/3}$ and the Debye length $\lambda_D = \sqrt{\epsilon_0\, k\, T/\, n\, q^2}$ are significantly smaller than the size of the cloud (where ϵ_0, k, T and q are the permittivity of free space, the Boltzmann constant, the temperature and the elementary charge, respectively). In our experimental conditions, where the electron densities are in the range of $n \approx 10^{14}$–$10^{15}\,\mathrm{m}^{-3}$, the Debye length is of the order of tens of microns only. We can thus expect that the plasma has a constant radial density profile, which then drops off to zero within a few Debye lengths around the plasma radius r_p defined as the point where the plasma density $n(r_p, 0) \equiv n_0/2$ is half the central one $n_0 \equiv n(0, 0)$.

Cold plasmas at thermal equilibrium can be considered a rigid rotor that rotates with frequency ω_r around the z-axis due to the presence of the axial magnetic field B and the radial electric field caused by the plasma's space-charge. The central density then follows [15]

$$n_0 = \frac{2m\epsilon_0\omega_r(\Omega_c - \omega_r)}{q^2}\,, \tag{1}$$

where $\Omega_c = qB/m$ is the particle cyclotron frequency. In our conditions, the plasma rotation frequency $\omega_r \ll \Omega_c$ and thus the above equation can be simplified to

$$\omega_r \cong \frac{qn_0}{2\epsilon_0 B}\,. \tag{2}$$

In the case of a mixed plasma composed of e^- and $\bar{p}$, the different charge-to-mass ratios of the two species makes them rotate around the axis at different speeds and thus the collisions between electrons and antiprotons tend to shift antiprotons to higher radii like in a centrifuge. This centrifugal separation effect depends on the temperature, the plasma radius and the density, and it becomes significant when the centrifugal potential difference for any of the species becomes larger than the thermal energy of the plasma [16]

$$|m_p - m_e|\frac{\omega_r^2\, r_p^2}{2} > k\, T. \tag{3}$$

From the above relations it is clear that for a given plasma radius the separation effect occurs either if the plasma is very cold or if the density is very high.[5] In our conditions, if no intentional heating signal is applied (see Sect. 4.2) during the initial $\bar{p}$ cooling process, the antiprotons start to centrifugally separate from the much lighter and denser electron cloud that cools them. This separation effect has been observed for example with laser-cooled positron–ion plasmas [17] or with electron-cooled antiprotons [18]. Figure 3 shows an example of such separation as seen in AEgIS on our MCP detector in case of a standard cooling and compression procedure described later in Section 4.2. Antiprotons at the end of that procedure were left to relax and drift toward the outer radii at the

[5] Ideally at thermal equilibrium the cold plasma of e^- and $\bar{p}$ rotates with a common rotation frequency ω_r and, depending on the level of separation, the central density n_0 can be composed of both electron and antiproton fractions, but since in our case electrons are the dominant species (more abundant by two orders of magnitude), we neglect the antiproton contribution to the density.

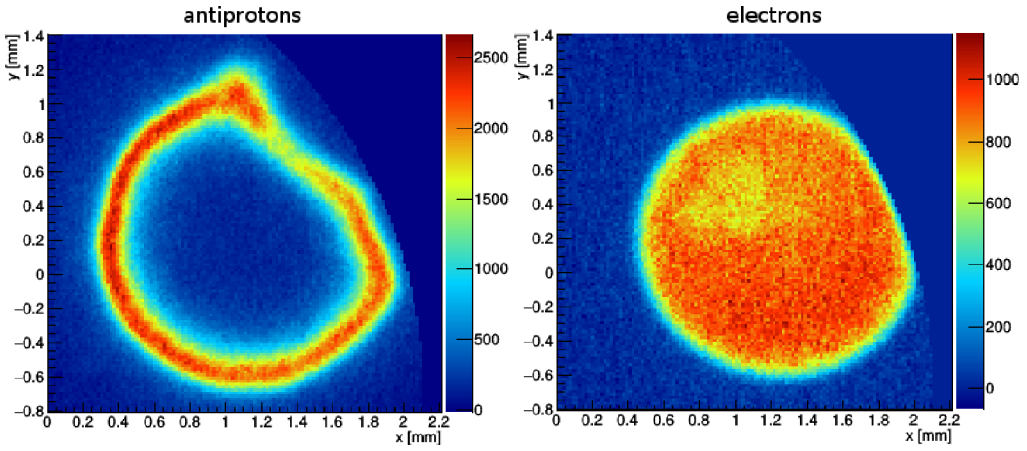

Fig. 3. Example of raw images from the MCP detector for identical particle operations with antiproton detection (left) or electron detection (right). The centrifugal separation effect between electrons and antiprotons is clearly visible. The origin is arbitrary, while the source of the distortion in the upper right quadrants is described in the text.

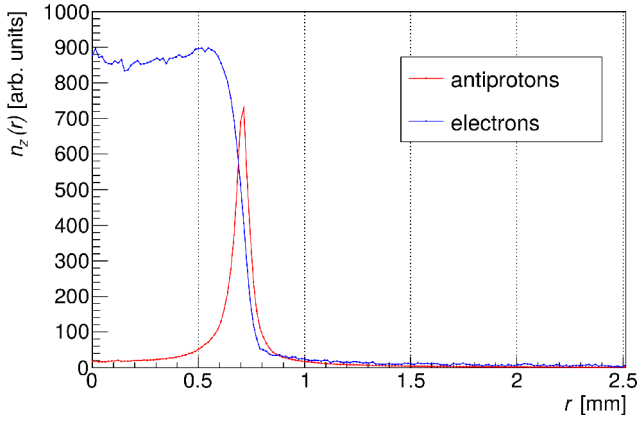

Fig. 4. The radial density profiles of the electron (blue) and $\bar{p}$ (red) clouds shown in Figure 3. The profiles were vertically scaled to fit the same range for comparison.

border of the electron plasma. The distortion from circular symmetry of both electron and antiproton images shown in Figure 3 is due to an off-center coaxial trap structure located between the P-trap and the MCP detector in the 1 T magnetic field. For fast electrons this structure causes a simple cut, while for the slower antiprotons even a single passage is sufficient to cause $E \times B$ drifts and, most likely, partially deform the shape due to the interaction of the $\bar{p}$ cloud with its own image charge. In the data analysis we excluded the deformed region of the image and performed a circular integral around the cloud center to obtain a (single pixel) weighted radial profile for each image.

Since we extract the particles along the magnetic field axis (z), the image of such particle clouds on the MCP detector is integrated along this axis leading to the measurement of the particle areal density $n_z(r) \equiv \int_z n(r,z)\,dz$. The radial profiles $n_z(r)$ of electrons and antiprotons corresponding to the measurements of Figure 3 are shown in Figure 4, where arbitrary units were used and the antiproton and electron profiles were arbitrarily scaled for better comparison. When radial density profile tails are discussed later in the text, the reader should bear in mind that the total number of particles N within some radius R is obtained by integrating the radial profile curve, leading to $N = \int_0^R 2\,\pi\,r\,n_z\,dr$. This expresses the simple fact that even small particle densities at large radii can contribute in a significant way to the total particle number and thus affect the overall compression efficiency.

Centrifugal separation is an unwanted effect since it causes a drift of $\bar{p}$ from the trap center into the regions of lower electron density. It does, however, allow setting limits on the particle temperature in our traps. Since electrons are the dominant species we estimate the electron plasma density from the electron number and the radius measurements by applying a numerical calculation [19] of the expected plasma length in the given trap vacuum potential.[6] From the knowledge of the electron density n_0 we calculate ω_r (from Eq. (2)) and use it, along with the measured radius, in equation (3) to obtain an upper or lower limit on the plasma temperature from the observation (an upper limit) or not (a lower limit) of the centrifugal separation effect (similarly as [18]). We estimate the best temperature of the antiproton–electron mixed plasma to be of the order of tens of kelvin in case no heating (RW) drive is applied. This is a rough order of magnitude estimate that assumes an ideal plasma in a thermal equilibrium, with both antiprotons and electrons having the same temperature.

4 Antiproton compression technique

The compression of the mixed plasma composed of $\bar{p}$ and e^- is performed by using the rotating wall RF signal as described in Section 2. A torque is transferred by the

[6] For practical computational reasons we have used as an input for the numerical calculation of the plasma equilibrium shape temperatures of 300 or 1160 K. As long as the Debye length is smaller than the plasma size the resulting calculated plasma lengths and densities vary only by a few percent. A calculated plasma length for a common space charge potential of ∼30 V is ≈12 cm and 5 cm for the long and short trap, respectively.

co-rotating electric field and causes the plasma to rotate faster. As the rotation frequency ω_r increases, so does the density n_0 in order to maintain the equilibrium condition of equation (2), leading to a reduction of the plasma radius.

4.1 Electron-only plasma RW compression

At first, we studied the RW compression of a pure electron plasma with the same initial loading conditions and trapping potentials as with a mixed $\bar{p}$ and e^- plasma. We define the plasma radius as the half-width-half-maximum (HWHM) of the radial density profile $n_z(r)$. This compression was carried out with a 2-step RW procedure in order to make the electron plasma initial condition similar to those in case of $\bar{p}$ trapping, cooling and compression. We first load e^- in the P-trap and then apply the rotating wall drive at $f_{\mathrm{RW}_1} = 0.3\,\mathrm{MHz}$ and $A_{\mathrm{RW}_1} = 3\,\mathrm{V}$ on two electrodes located in the center of the trap. The application of this first step is important for two reasons. The first is the need to adjust the initial electron cloud to the size used in antiproton experiments and the second is that while working with antiprotons, the RW drive itself is used as a heating source to overcome the centrifugal separation effect described in Section 3. After having reached equilibrium with the applied drive within ≈10–20 s (depending on the initial loading conditions), the plasma radius no longer changes. We then apply a second RW step for 20 s at a higher frequency $f_{\mathrm{RW}_2} \geq f_{\mathrm{RW}_1}$. The compression achieved at the end of the second step as a function of the applied RW frequency is shown in Figure 5, where two electron clouds that differ in electron number N_{e^-} (and consequently also in initial size) were studied. We observed losses of particles for higher frequencies, accompanied by a reduction of peak density and plasma broadening. Such losses are probably space-charge related and caused by the necessity to shift the plasma into a shorter and shallower potential prior to extraction (blue curve in Fig. 2). In fact, for the peak compressions we estimate the plasma to occupy the full length of the final trap and have a space-charge potential a few volts below the on-axis trapping potential. Interestingly, we observed that for both of the electron clouds the maximum density reached with the RW drive (in the absence of losses) was approximately the same and of the order of $n \approx 10^{15}\ \mathrm{m}^{-3}$. This hints at a possible RW compression density limit in our case and it thus helps to explain why plasmas with a lower electron number have a minimum achievable radius smaller than plasmas with a higher electron number.

Turning on the RW drive in a step-like fashion on a slowly rotating plasma causes significant axial heating (in the first 100 ms of operation), which leads to axial electron losses. A similar heating effect has been previously observed [11]. For this reason, we used a ∼300 V deep trapping potential at the beginning of the RW application (the trapping potential can be restored afterwards to lower values). Since we do not observe a linear relationship (similar to Eq. (2)) between the plasma density and the applied RW frequency, we believe that we are not in the so-called "strong drive" RW regime [20], which is characterized by the plasma rotation frequency ω_r being equal

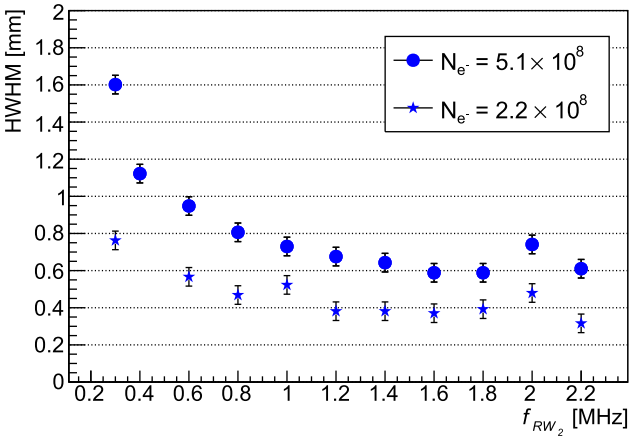

Fig. 5. Electron cloud radii (HWHM) vs. applied RW_2 frequency in a two step compression procedure in the absence of antiprotons. The two data sets differ in the initial electron loading conditions.

to the applied RW drive frequency ω_{RW}. The behavior we observe is rather similar to the "weak" drive seen in similar experiments [10], where compression occurs in a broad range of frequencies, but stops working at higher frequencies. The most probable cause is an excessive plasma heating by the RW drive and the plasma modes' decoupling from the applied drive.

4.2 Single step compression of $\bar{p}$ and e^-

In order to compress the mixed $\bar{p}$ and e^- plasma that we obtain after antiproton catching and cooling (see Sect. 2), we find that the most important aspect is to avoid the centrifugal separation effect. As we have discussed in Section 3, this separation effect causes a drift of $\bar{p}$ towards larger radii. To overcome this effect one has two options (as can be inferred from Eq. (3)): either reduce the electron plasma density or increase the plasma temperature. For fast antiproton cooling from keV energies down to the eV range, a high electron density is necessary, but temperatures below 1 eV are not required for the compression stages since the trapping potential is of the order of 100 V. As we estimate (see Sect. 3) the plasma temperature to ultimately reach (once RF heating is turned off) on the order of a few meV, we applied a plasma heating signal to overcome the centrifugal separation effect during the compression stage. Due to initial hardware limitations we used the RW drive itself as a means of plasma heating, but other heating techniques [21] can be implemented in the future. For this heating purpose we kept the initial preparatory electron RW_1 drive turned on also during the antiproton catching and cooling procedure, such that cold antiprotons would not drift to outer radii, but instead remain homogeneously mixed within the electron plasma.

The antiproton compression starts after the release of the uncooled antiproton fraction. Usually the drive was kept at $f_{\mathrm{RW}_1} = 300$–$400\,\mathrm{kHz}$ and $A_{\mathrm{RW}_1} = 2\,\mathrm{V}$ and did not cause further compression since the electron plasma reached the equilibrium density (and radius) ≈20 s before the arrival of antiprotons. The drive ensures that the

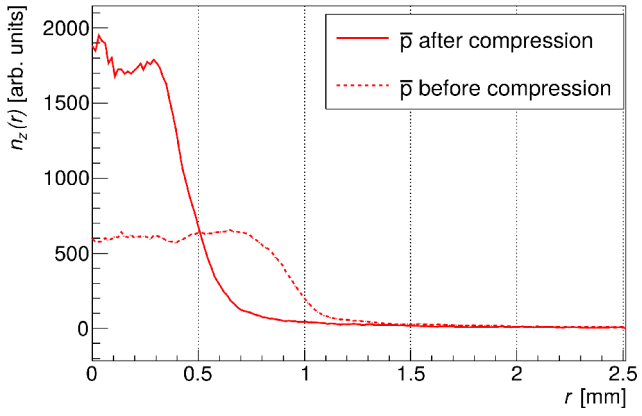

Fig. 6. An example of single step $\bar{p}$ RW compression. Radial profiles of antiprotons are shown before (dotted line) and after (full line) compression for 20 s with $f_{\mathrm{RW}_2} = 1.5$ MHz, $A_{\mathrm{RW}_2} = 2$ V, $N_{e^-} = 2 \times 10^8 e^-$. The $\bar{p}$ radii were 0.96 mm before and 0.46 mm after compression.

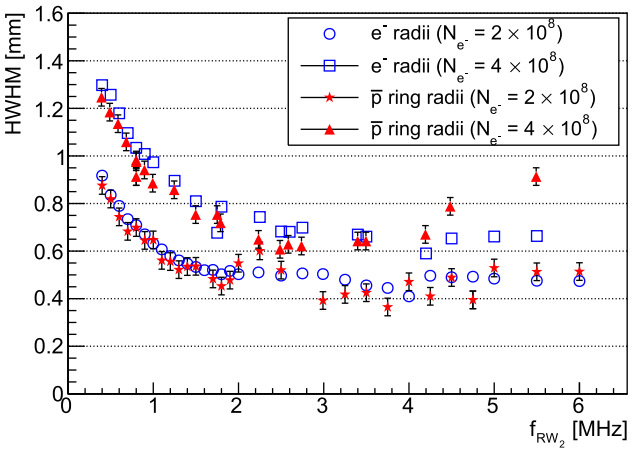

Fig. 7. Single step $\bar{p}$ RW compression. Electron and antiproton radii are plotted as a function of f_{RW_2} for two e^- loading conditions.

mixed plasma retains a constant dimension, preventing a possible expansion of both species. At this point, we start compressing the e^- and $\bar{p}$ by changing the RW frequency and amplitude to new values f_{RW_2} and A_{RW_2}. An example of such compression of the antiproton radial density profile is shown in Figure 6, where a compression factor of 2 was achieved after 20 s application of $f_{\mathrm{RW}_2} = 1.5$ MHz, $A_{\mathrm{RW}_2} = 2$ V. To avoid possible on-axis losses at RW stepwise start, we raised the endcap potentials of the trap right before the application of the RW_2 step (from green to red curve in Fig. 2). In Figure 7 we show the dependence of the electron and antiproton radii on the RW_2 drive frequency for either $N_{e^-} = 2 \times 10^8$ or $N_{e^-} = 4 \times 10^8$ loaded in the trap. Irrespective of the number of electrons used, we reach approximately the same e^- final density; this leads to smaller antiproton clouds if less electrons are loaded.[7] The behavior of the $\bar{p}$ radius follows that of the electrons, which are compressed in a similar manner as for an electron-only plasma (Fig. 5). The maximum compression is reached at $f_{\mathrm{RW}_2} = 2$–4 MHz, similar to electron-only compression. At high frequencies, excessive heating and partial on-axis losses (facilitated by the higher space-charge of the plasma) occur. The compression limit above $f_{\mathrm{RW}_2} > 4$ MHz is thus most probably related to the space-charge losses in the final (shorter and shallower) trap configuration used for particle extraction (blue curve in Fig. 2).

The compression of antiprotons in the procedure described above takes place from the moment we increase the RW drive frequency, which causes the electron plasma to increase its rotation frequency and consequently decrease in size. The $\bar{p}$ follow the electrons in case the compression is sufficiently slow; otherwise, part of the $\bar{p}$ cloud remains at large radii (the electron core should reach the peak density on a time scale not shorter than 15–20 s in agreement with [22]). The RW compression rate has to be controlled by correctly adjusting the amplitude of the RW drive while compressing the mixed antiproton–electron plasma. Figure 8 shows the antiproton profiles obtained after one such $\bar{p}$ RW compression, for different RW drive amplitudes.

The profiles shown in Figures 8 and 9 are hollow due to centrifugal separation, because during these measurements the RW_2 drive was turned off 2 s before reshaping the trap into the shorter configuration (which took 1.5 s) and then particles remained in the short trap for 2 s until the extraction took place. We estimate (from [23]) the time necessary for the centrifugal separation to occur to be of the order of 4 s in the long trap configuration ($n \approx 1.1 \times 10^{15}$ m^{-3}, $T \approx 4$ meV and $r_p \approx 0.9$ mm) and approximately half as much in the shorter trap (where the density is twice as high).[8] In other works with similar multispecies systems [22,24] the reported separation times were significantly shorter than those theoretically expected in [23] or [25]. As we can only set an upper limit of ~2 s in our case, we cannot exclude that the centrifugal separation time has been significantly lower than that. Recently, diocotron plasma modes have been proposed as a possible cause for an enhanced centrifugal separation rate [24], but unfortunately we did not monitor the plasma's modes activity during these measurements.

The centrifugally separated images can still be used to evaluate the level of compression, as we observed that the $\bar{p}$ ring radius is the same as the $\bar{p}$ HWHM in case of no centrifugal separation. In Figure 8 we observe that the $\bar{p}$ density distribution $n_z(r)$ has more pronounced tails in case of higher A_{RW_2}. Lower amplitude (and thus slower) compression favors a denser $\bar{p}$ core and thus improves the overall compression efficiency. The compression shown in Figure 8 was not performed in the optimal settings; in fact the initial electron plasma rotated at approximately $f_r = \omega_r/2\pi = 150$ kHz, and directly applying a 3 MHz RF drive causes some of the antiprotons to remain in

[7] It should be noted though that in the case of 2×10^8 e^- the $\bar{p}$ cooling efficiency from keV energies drops with respect to the case with 4×10^8 e^- due to the smaller e^- and $\bar{p}$ cloud geometrical overlap.

[8] We have also observed centrifugal separation in similar cases where the RW drive was turned off just before the 1.5 s of reshaping and 2 s of waiting before the extraction.

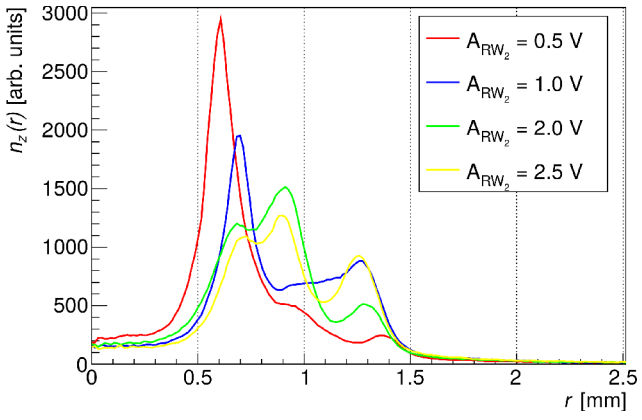

Fig. 8. Antiproton radial profiles after the single step $\bar{p}$ RW compression at $f_{\mathrm{RW}_2} = 3\,\mathrm{MHz}$ for different drive amplitudes A_{RW_2}. The ring structures are due to the centrifugal separation caused by a delay between turning off the RW drive (heating) and particle extraction. Lower amplitudes favor smaller $\bar{p}$ tails.

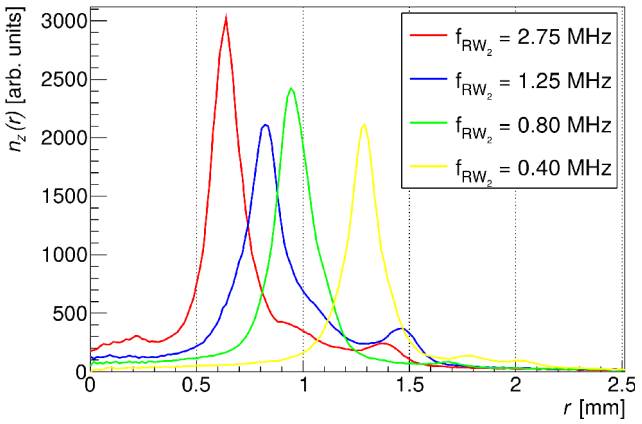

Fig. 9. Antiproton radial profiles during the single step RW compression for various f_{RW_2} while keeping $A_{\mathrm{RW}_2} = 0.5\,\mathrm{V}$ fixed. The yellow curve ($f_{\mathrm{RW}_2} = 0.4\,\mathrm{MHz}$) is the initial condition without the $\bar{p}$ compression step.

the tails. This effect can be seen in Figure 9, where for a fixed amplitude of $A_{\mathrm{RW}_2} = 0.5\,\mathrm{V}$ the frequency of the drive was varied. With respect to the initial conditions (yellow curve), the lowest tail population is observed for $f_{\mathrm{RW}_2} = 0.8\,\mathrm{MHz}$, which is double the initial RW drive frequency of 400 kHz. Even though 0.8 MHz clearly did not show the highest $\bar{p}$ core compression, the tails were the lowest. The importance of the tail distributions is discussed in greater detail in Section 5.

4.3 Multi-step $\bar{p}$ and e^- plasma compression

The single step antiproton compression shown in the previous section is sufficient for many applications where it is necessary to reduce the antiproton cloud radial size. However, it is not sufficient to obtain a cold antiproton plasma where higher densities are necessary. In order to do so we have developed a multi-step $\bar{p}$ RW compression method based on alternating electron number reduction and compression cycles. This method was chosen based on the previous experience (for example in Fig. 7), where the single step $\bar{p}$ RW compression procedure showed a limit in the maximum electron density rather than in the radius or particle number. The simplest of such multi-step procedures consisted of one intermediate electron number reduction step immediately after the initial $\bar{p}$ capture and cooling. The procedure was similar to the one described in the preceding section, where $f_{\mathrm{RW}_1} = 0.3$–$0.4\,\mathrm{MHz}$ was applied right after electron loading and maintained until the uncooled $\bar{p}$ fraction release. We then reshaped the trap and split it axially (red dotted curve in Fig. 2), such that only 1/5 of electrons ($N_{e^-} \approx 7.6 \times 10^7$) remained intact and the rest was removed with three 80 ns voltage pulses applied on one endcap. At this moment we also turned off the f_{RW_1} drive, which was used both to keep the radius constant and as a heating mechanism. The trap was then restored to its original full length of ten electrodes and returned to its deep configuration (red curve in Fig. 2). After such a dramatic electron reduction, and thus a decreased electron density, the centrifugal separation effect was not observed. The shape of the remaining $\bar{p}$ and e^- cloud changed slightly due to this electron removal and potential reshaping procedure, leading to an electron HWHM of ≈1.3 mm and a small tail growth. We then applied two successive frequency steps RW_2 and RW_3 of the rotating wall drive. The choice of two frequency steps instead of one was based on the experience gained from measurements like those shown in Figure 9, where we observed that for slowly rotating plasmas it is better to first apply an intermediate frequency step in order to limit the creation of tails in the radial density distribution. Due to the effect described above we also performed preliminary trials using a swept RF drive (in both frequency and amplitude) instead of a step-wise application, but we did not observe a significant improvement with respect to the step-wise application. Nonetheless, we believe that a deeper dedicated study on this topic would be of great importance if it is demonstrated that the swept RW drive compression is faster or more efficient with respect to a step-wise RW application.

After the reduction of the number of electrons we started to compress the antiprotons by applying a rather low frequency $f_{\mathrm{RW}_2} = 200\,\mathrm{kHz}$ with $A_{\mathrm{RW}_2} = 2\,\mathrm{V}$. Once the maximum compression was reached for this frequency (after ≈20 s) we applied a second $\bar{p}$ RW compression step (for ≈40 s) within the range $f_{\mathrm{RW}_3} = 0.2$–$5\,\mathrm{MHz}$, and with lower amplitude $A_{\mathrm{RW}_3} = 0.5\,\mathrm{V}$, in order to avoid tail creation and inefficient compression as observed in the example of Figure 8. The radii of the $\bar{p}$ and e^- clouds as a function of f_{RW_3} can be seen in Figure 10. At frequencies exceeding 4 MHz the heating effect of the RW drive becomes significant and causes broadening of the antiproton/electron cloud, losses and tail growth. As can be seen in Figure 10, a maximum radius compression factor of 5 was reached. We estimate the maximum plasma space charge potential to be of the order of 30 V for the best compressions and thus the compression limit seen in Figure 10 is not caused by an insufficient final trapping potential. The interesting aspect shown in Figure 10 is that the final antiproton cloud radius can be chosen

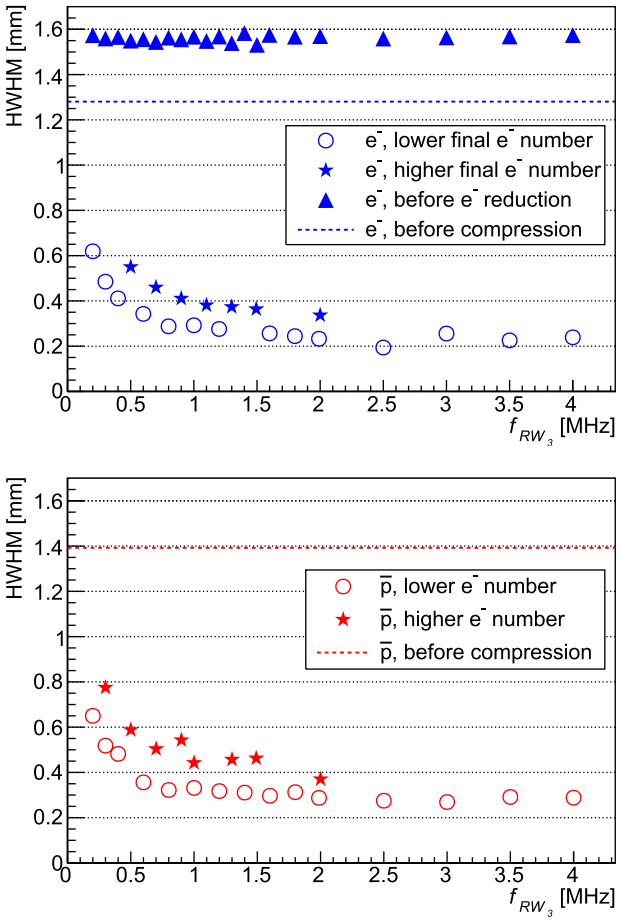

Fig. 10. HWHM of electrons (top panel) and antiprotons (bottom panel) vs. f_{RW_3} during the two-step $\bar{p}$ RW compression procedure. When more electrons remain in the trap after the partial e^- removal (stars) compression is less pronounced. The dotted lines indicate the particle cloud radius after the e^- reduction before turning on the RW drive.

by applying the corresponding RW frequency f_{RW_3} that was found previously with electron-only experiments. As expected from the previous findings, one can observe that if more electrons remain in the trap during the compression stages the minimum radius reached is larger than if less electrons remain in the trap.

Thus, to attempt achieving even higher compression, we added another electron number reduction step as well as one more compression step RW_4. We performed the same procedure as the one of Figure 10, but instead of removing all the electrons while located in the final shortened trap (blue curve of Fig. 2) we removed only a fraction and then turned on the last $\bar{p}$ RW drive at a relatively high frequency. We applied the final RW_4 step in a shorter trap; right before the final particle extraction, the plasma is thus located in a potential created by five 13.5 mm electrodes instead of ten electrodes. The position of the RW electrodes is towards one side of the trap, instead of the central position it had in the previous steps (RW_1–RW_3). Figure 11 shows the radial density profiles of the antiprotons before and after the best RW_4 compression with

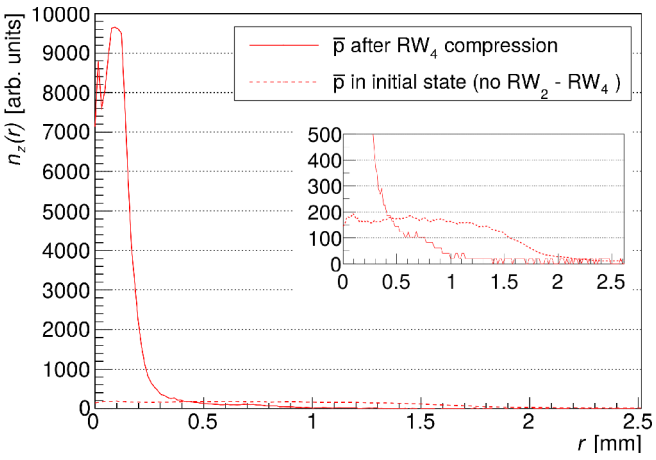

Fig. 11. Antiproton radial profile before (dotted line) and after (solid line) multi-step RW compression with $f_{\mathrm{RW}_4} = 2\,\mathrm{MHz}$ and $A_{\mathrm{RW}_4} = 0.5\,\mathrm{V}$. The inset is a zoom of the same figure to show the original $\bar{p}$ distribution before compression. During this procedure two e^- reduction steps were applied and in total three $\bar{p}$ RW compression steps were used. The $\bar{p}$ HWHM was 1.63 mm before and 0.17 mm after the compression.

$f_{\mathrm{RW}_4} = 2\,\mathrm{MHz}$ and $A_{\mathrm{RW}_4} = 0.5\,\mathrm{V}$. During this multi-step RW procedure with two partial electron removal steps and three $\bar{p}$ compression steps, the final antiproton cloud radius was found to be $r_{\bar{p}} = 0.17\,\mathrm{mm}$, which is an almost tenfold improvement with respect to the initial $\bar{p}$ radius of 1.63 mm.

The application of the RW steps in the procedures presented caused in total between 25% and 35% loss of antiprotons. Of these losses, ≈7% can be attributed to the way we remove the electrons (see Sect. 2). Since it is impossible to detect electrons and antiprotons simultaneously on the MCP, this forces us to completely remove the electrons from the trap with an excessive number of voltage pulses, during which some of the antiprotons are lost. This loss mechanism is also present in the partial electron removal pulses that are necessary for successful compression, but to a limited extent since not all the e^- need to be extracted in those cases.

Together with a decrease of the $\bar{p}$ plasma radius by a factor 9.6, the peak density has increased approximately by a factor 55, as can be seen in Figure 11. Approximately 2/3 of the compressed antiprotons of Figure 11 are located within the measured HWHM. With the multi-step compression method described above we estimate ≈70 000 $\bar{p}$ within the 0.17 mm radius and an antiproton density of the order of $n_{\bar{p}} = 2 \times 10^{13}\,\mathrm{m}^{-3}$. This is to our knowledge the smallest antiproton cloud radius and the highest antiproton density reported so far in a Penning–Malmberg trap.

5 Necessary conditions for high-density $\bar{p}$ plasma preparation

During our studies, we have performed RW compression of $\bar{p}$ plasmas under various conditions and in different trap lengths. The rotating wall compression depends on many

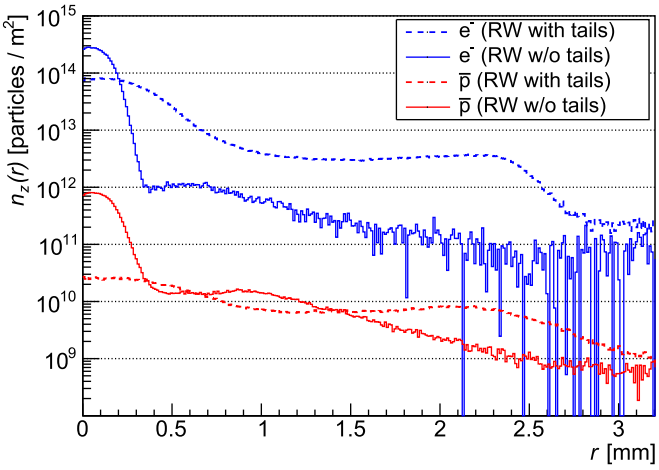

Fig. 12. Radial density profile of e^- and $\bar{p}$ after two cases of RW compression. Dotted lines show unsuccessful compression while the full lines show the high-density $\bar{p}$ compression example. Because of the limited dynamic range of the MCP, the high-density electron curves show higher noise at large radii with respect to the lower density $\bar{p}$ profiles.

factors. To reach high compression ratios each apparatus or trap system needs its own specific commissioning and testing phase and results might differ from one apparatus to another. During the measurements presented here, the conditions did change a few times and it was thus necessary to re-establish good compression parameters on several occasions. Thus, we established a set of conditions that seem to be necessary to reach high antiproton compression ratios.

As was discussed in Section 4.2, it is essential to work at temperatures (or densities) where the centrifugal separation of antiprotons and electrons is absent. Otherwise, large portions of antiprotons drift outwards and remain at large radii even though the electrons might be compressed effectively.

We observed antiproton-only expansion and successive losses both in long and short trap configurations when using f_{RW} below 200 kHz. This low frequency loss effect probably depends on e^- plasma density and size, but we were unable to identify a clear dependence. We saw day-to-day variations of these losses at lower frequencies and, in general, found less losses when starting the RF drive on initially less dense antiproton–electron plasmas.

The most important condition to achieve maximal antiproton compression, irrespective of the exact RW procedure applied, is to reduce the electron cloud tail density to a minimum. To quantify this effect we use a peak-to-tail density ratio that we define as $n_{p/t} \equiv n_z(0)/n_z(r_t)$ with $r_t \equiv 3\,r_{\mathrm{HWHM}}$ being the radial tail position defined as three times the HWHM radius. This choice was deliberate since in our apparatus an ideal non-neutral plasma in a global thermal equilibrium would have more than 99% particles within r_t, which is not the case for the particle clouds that we observe. We found that for efficient antiproton compression the peak-to-tail density ratio for electrons should be of the order of $n^{e^-}_{p/t} \approx 150$ or higher to achieve a high core density antiproton plasma. To illustrate this effect we show an example of efficient and inefficient $\bar{p}$ compression in Figure 12, where we see that the antiproton radial density profiles copy relatively well those of the electrons, with the difference that antiprotons tend to populate more the lower density regions and have a lower peak-to-tail ratio than electrons. As can be seen in Figure 12, in the case of one of the best compressions, the electron ratio is $n^{e^-}_{p/t} = 190$, whereas the corresponding antiproton profile shows $n^{\bar{p}}_{p/t} = 47$.

We found that at higher RW amplitudes (above 0.5 V) the electron core compressed well, but some electron tails remained. The antiprotons were then more evenly distributed and in some cases like that shown in Figure 12 (dotted lines) there was practically no antiproton compression (with $n^{\bar{p}}_{p/t} \approx 3.6$ and $n^{e^-}_{p/t} \approx 23$). For this reason we believe that the necessity to compress the $\bar{p}$ and e^- plasma slowly (with low amplitudes) is dictated by the need to compress electrons without creating tails. To achieve a high $\bar{p}$ peak-to-tail compression ratio it is important to reduce the electron tail density to a factor ≈50 of that of the requested antiproton tail density. We suspect that the ideal compression would occur in case one could create a dense compressed core with the required radius and at the same time maintain an electron tail density $n \leq 10^{11}\,\mathrm{m}^{-3}$.

We suspect that the electron tails we observe are the remnants of the original electron cloud distribution prior to the RW application. In fact, such tails are visible also in the case of pure electron plasma compression, in some cases tails take the form of a pedestal or a ring that have approximately the radius of the original uncompressed electron plasma (prior to the RW drive application). It seems to us that a possible way to solve the e^- and $\bar{p}$ mixed plasma RW compression problem could be through a detailed study of the low-density tails of electron plasmas, such as the recently studied dynamics of "halos" [26], but in the presence of both dipolar or quadrupolar RW excitations.

In all RW experiments that we have conducted we never managed to fully compress all particles within r_t. Either we had ≈30% losses – mostly in the tails – and ≈2/3 of $\bar{p}$ within the HWHM or we achieved lossless compression with roughly 33% of $\bar{p}$ inside the HWHM. We obtain density increase factors in the range 30–55 and $\bar{p}$ densities $n_{\bar{p}} \geq 10^{13}\,\bar{p}/\mathrm{m}^3$ with ≈70 000 $\bar{p}$ within radii as low as 0.17 mm in 4.46 T traps. Since in these conditions the antiproton cloud has an estimated Debye length $\lambda_D \approx 100\,\mu$m and an interparticle spacing $n^{-1/3}$ of tens of microns it can be considered a cold antiproton non-neutral plasma.

6 Conclusions

We performed compression of a mixed $\bar{p}$ and e^- plasma trapped in a cryogenic Penning–Malmberg trap and achieved high antiproton densities ($n_{\bar{p}} \sim 10^{13}\,\mathrm{m}^{-3}$) by using the rotating wall method. The compression procedure was accompanied by partial electron number reduction to achieve the lowest $\bar{p}$ radii of $r_{\bar{p}} = 0.17$ mm.

The final $\bar{p}$ radius can be tuned based on the RW frequency applied. We described in detail the necessary conditions for compression of antiprotons, the most important of which is the requirement to compress with high efficiency the electron cloud, including possible electron tail structures that might remain at larger radii. Such electron tails may have been overlooked in past works on rotating wall drive compression, as the main interest was in the description of the peak (central) plasma density or the HWHM observable. The observations described in this work are of great importance for any experiment that needs to effectively reduce the radius of a trapped antiproton cloud, also because it was shown that the major preparatory work can be done with pure electron plasmas and thus conserve important antiproton beamtime.

The small dimension ($r_{\bar{p}} = 0.17\,\mathrm{mm}$) and high number (70 000) of antiprotons available allow for a lossless transport into a lower magnetic field and pave the way to an efficient production of antihydrogen in the AE$\bar{\mathrm{g}}$IS apparatus.

This work was supported by Istituto Nazionale di Fisica Nucleare; the Swiss National Science Foundation Ambizione Grant (No. 154833); a Deutsche Forschungsgemeinschaft research grant; an excellence initiative of Heidelberg University; Marie Skłodowska-Curie Innovative Training Network Fellowship of the European Commission's Horizon 2020 Programme (No. 721559 AVA); European Research Council under the European Union's Seventh Framework Program FP7/2007-2013 (Grants Nos. 291242 and 277762); Austrian Ministry for Science, Research, and Economy; Research Council of Norway; Bergen Research Foundation; John Templeton Foundation; Ministry of Education and Science of the Russian Federation and Russian Academy of Sciences; and the European Social Fund within the framework of realizing the project, in support of intersectoral mobility and quality enhancement of research teams at Czech Technical University in Prague (Grant No. CZ.1.07/2.3.00/30.0034).

Author contribution statement

D.K. and G.T. conceived and planned the experiments. D.K. analyzed the data and wrote the manuscript with input from all authors. G.T. supervised the findings of this work. All authors contributed to data-taking and provided critical feedback.

References

1. M. Amoretti et al., Nature **419**, 456 (2002)
2. G. Gabrielse et al., Phys. Rev. Lett. **89**, 213401 (2002)
3. M. Doser et al., Class. Quantum Grav. **29**, 184009 (2012)
4. P. Perez, Y. Sacquin, Class. Quantum Grav. **29**, 184008 (2012)
5. E. Widmann et al., Hyperfine Interact. **215**, 1 (2013)
6. M. Ahmadi et al., Nature **541**, 506 (2017)
7. M. Amoretti et al., Phys. Lett. A **360**, 141 (2006)
8. J. Fajans et al., Phys. Rev. Lett. **95**, 155001 (2005)
9. X.-P. Huang et al., Phys. Rev. Lett. **78**, 875 (1997)
10. E.M. Hollmann, F. Anderegg, C.F. Driscoll, Phys. Plasmas **7**, 2776 (2000)
11. J.R. Danielson, C.M. Surko, T.M. O'Neil, Phys. Rev. Lett. **99**, 135005 (2007)
12. G.B. Andresen et al., Phys. Rev. Lett. **100**, 203401 (2008)
13. D. Krasnický et al., AIP Conf. Proc. **1521**, 144 (2013)
14. B.R. Beck, J. Fajans, J.H. Malmberg, Phys. Plasmas **3**, 1250 (1996)
15. D.H.E. Dubin, T.M. O'Neil, Rev. Mod. Phys. **71**, 87 (1999)
16. T.M. O'Neil, Phys. Fluids **24**, 1447 (1981)
17. B.M. Jelenković et al., Phys. Rev. A **67**, 063406 (2003)
18. G. Gabrielse et al., Phys. Rev. Lett. **105**, 213002 (2010)
19. R.L. Spencer, S.N. Rasband, R.R. Vanfleet, Phys. Fluids B **5**, 4267 (1993)
20. J.R. Danielson, C.M. Surko, Phys. Rev. Lett. **94**, 035001 (2005)
21. B.P. Cluggish, J.R. Danielson, C.F. Driscoll, Phys. Rev. Lett. **81**, 353 (1998)
22. G.B. Andresen et al., Phys. Rev. Lett. **106**, 145001 (2011)
23. D.H.E. Dubin, AIP Conf. Proc. **1521**, 26 (2013)
24. A.A. Kabantsev, K.A. Thompson, C.F. Driscoll, AIP Conf. Proc. **1928**, 020008 (2018)
25. M. Amoretti et al., Phys. Plasmas **13**, 012308 (2006)
26. A.A. Kabantsev, C.Y. Chim, T.M. O'Neil, C.F. Driscoll, Phys. Rev. Lett. **112**, 115003 (2014)